Additive Manufacturing 28 (2019) 517–527

Contents lists available at ScienceDirect

Additive Manufacturing

journal homepage: www.elsevier.com/locate/addma

Full Length Article

Interrupted fatigue testing with periodic tomography to monitor porosity defects in wire + arc additive manufactured Ti-6Al-4V

Romali Biswal[a], Xiang Zhang[a,*], Muhammad Shamir[a], Abdullah Al Mamun[b,1], Mustafa Awd[c], Frank Walther[c], Abdul Khadar Syed[a]

[a] Faculty of Engineering, Environment and Computing, Coventry University, Coventry, CV1 5FB, UK
[b] Engineering and Innovation, The Open University, Walton Hall, Milton Keynes, MK7 6AA, UK
[c] Department of Materials Test Engineering, TU Dortmund University, 44227 Dortmund, Germany

ARTICLE INFO

Keywords:
Additive manufacturing
Porosity defects
X-ray computed tomography
Finite element modelling
Fatigue life prediction
Titanium alloy

ABSTRACT

Porosity defects remain a challenge to the structural integrity of additive manufactured materials, particularly for parts under fatigue loading applications. Although the wire + arc additive manufactured Ti-6Al-4 V builds are typically fully dense, occurrences of isolated pores may not be completely avoided due to feedstock contamination. This study used contaminated wires to build the gauge section of fatigue specimens to purposely introduce spherical gas pores in the size range of 120–250 micrometres. Changes in the defect morphology were monitored via interrupted fatigue testing with periodic X-ray computed tomography (CT) scanning. Prior to specimen failure, the near surface pores grew by approximately a factor of 2 and tortuous fatigue cracks were initiated and propagated towards the nearest free surface. Elastic-plastic finite element analysis showed cyclic plastic deformation at the pore root as a result of stress concentration; consequently for an applied tension-tension cyclic stress (stress ratio 0.1), the local stress at the pore root became a tension-compression nature (local stress ratio −1.0). Fatigue life was predicted using the notch fatigue approach and validated with experimental test results.

1. Introduction

Additive manufacturing (AM) technology supports the existing capabilities of the manufacturing industry with advantages of material savings and unparalleled design freedom. However, AM processed parts are also subjected to a complex thermal history, which can vary the microstructure from part to part and even from location to location within the same part [1]. Furthermore, process-induced defects are a major concern due to their effect on the fatigue performance in the powder bed fusion processes (such as the selective laser melting [2,3], electron beam melting [4,5]) as well as the directed energy deposition processes (such as the powder based direct laser deposition [6], wire + arc AM [7,8], and laser metal-wire deposition [9,10]). A recent study [11], using in-situ X-ray synchrotron imaging monitored the melt pool solidification and porosity evolution during electron beam melting of Ti-6Al-4V and concluded that centrifugal Marangoni convention force drives the entrapped gas pores in the melt pool. This is evidence of the high probability of gas pore entrapment in the melt pool, and therefore it is important to understand the impact of gas pores on the fatigue behaviour.

The presence of porosity defects causes stress concentration that depends on the pore characteristics, i.e. the size, shape and location. Ti-6Al-4V exhibits low work hardening as the difference between the material's yield strength and the ultimate tensile strength is relatively small [7,12], which indicates that the material is sensitive to stress raisers such as pores. Further, depending on the size of the pore in comparison to the surrounding microstructure, it can either act as a microscopic or a macroscopic stress raiser [13]. According to a study on wrought Ti-6Al-4V [14], when the ratio of defect size to the α colony size is within a factor of 8, it can be treated as microscopic defect. Conversely, any defect greater than this size can be treated as macroscopic defects. The sensitivity of Ti-6Al-4V to microscopic defects is low, as the microscopic barriers help in arresting the crack [15]. However, macroscopic defects can be adverse for fatigue applications due to the stress concentration and plastic deformation at the pore root.

X-ray computed tomography (X-ray CT) is one of the advanced non-destructive techniques being utilised for analysing defect characteristics. In an early study on a cast aluminium alloy [16], in-situ fatigue

* Corresponding author.
E-mail addresses: biswalr@uni.coventry.ac.uk (R. Biswal), xiang.zhang@coventry.ac.uk (X. Zhang).
[1] Present address: Department of Mechanical Engineering, University of Bristol, Bristol BS8 1TR, UK.

https://doi.org/10.1016/j.addma.2019.04.026
Received 24 January 2019; Received in revised form 30 April 2019; Accepted 30 April 2019
Available online 01 May 2019

testing was conducted with periodic X-ray CT scanning on cylindrical fatigue specimens. It was observed that the fatigue crack advanced at a higher rate in the vicinity of defects. Tammas-Williams et al. [17] investigated the crack initiation and crack growth from near spherical pores in electron beam melted Ti-6Al-4V. It was found that substantially smaller surface defects caused fatigue crack initiation even in the presence of larger pores located at internal sites which had a higher value of stress intensity factor (calculated according to Murakami's approach [18]). This can be due to the lower activation energy required for dislocation movement among the surface grains, which made fatigue crack initiation easier on the surface [19]. However, the detection of crack initiation using X-ray CT technique remains a challenge as the cracks may not be detected until the crack opening displacement reaches the minimum detection resolution (around 20–30 mm) [17].

Predictive models based on a defect tolerant design approach, such as Murakami's [18] and El-Haddad's [20] models, are widely used [3,21–23] to determine the effect of defects on the fatigue limit of AM materials, where the defect is assumed as a crack. However, gas pore morphology differs significantly from that of a crack, which can cause conservative predictions as reported in [17,22]. Probabilistic approaches are frequently applied for aluminium alloys [24–27] due to the higher porosity volume. In contrast, titanium alloys, particularly wire + arc additive manufactured Ti-6Al-4V, exhibit few isolated pores [7], which suggests that probabilistic models may not be ideal. Models based on the stress concentration effect, also referred to as notch fatigue approach, have been applied for macro-scale stress raisers, e.g. notches and corrosion pits [28–31]. The approach was also applied in a previous study for fatigue life prediction in the presence of isolated gas pores in SLM Ti-6Al-4V [32]. Further, the use of advanced constitutive models with mixed isotropic and kinematic hardening have been reported to improve the prediction accuracy of the notch fatigue method [28,32].

The present study aims at investigating the changes in the morphology of pores under fatigue loading in wire + arc additive manufactured titanium alloy (WAAM Ti-6Al-4V). Interrupted fatigue testing was performed at an applied stress amplitude of 315 MPa and stress ratio of 0.1, with a periodic X-ray CT scanning of the pores in the specimen gauge section to observe the crack initiation from the critical pores with increasing fatigue cycles. Finite element (FE) analysis was conducted to determine the stress concentration factor value using the X-ray CT image generated model and later compared to FE models with idealised pore geometries. Elastic-plastic cyclic load FE analysis was performed with a mixed isotropic-kinematic model to calculate the nonlinear cyclic response of WAAM Ti-6Al-4V. Local stress values determined by the FE model were used in the notch fatigue method to predict the fatigue life of the specimen. The prediction method was validated by the experimental results.

2. Experimental details

2.1. Manufacturing

Wire + arc additive manufactured wall was deposited at Cranfield University on a HiVE machine (High-Value Engineering) using Ti-6Al-4V wire feedstock (AWS 5.16- grade 5, 1.2 mm diameter). Two types of walls were deposited using optimised processing parameters given in Table 1. The two walls were referred to as: (a) reference wall, shown in Fig. 1(a), deposited using the standard clean wire, and (b) porosity wall, shown in Fig. 1(b), using a contaminated wire to deposit the mid-section of the wall such that the extracted fatigue specimens were expected to contain pores in the gauge section. The wire was contaminated using water displacement 40th formula (WD-40®) as described in detail in a previous work [33].

Table 1
Parameters used for material deposition.

Current (A)	210
Torch stand-off (mm)	8
Travel speed (m/min)	3.5
Plasma gas (l/min)	0.8
Plasma shield (l/min)	10
Trailing shield (l/min)	200

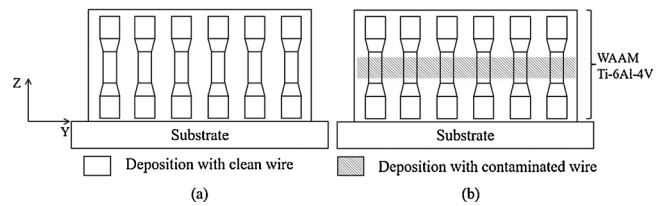

Fig. 1. Specimen extraction strategy: (a) reference specimens, (b) porosity specimens.

2.2. Cyclic load test for stress-strain relationship

Displacement controlled cyclic load test specimens were extracted from the reference wall in vertical orientation with respect to the build direction and machined according to ASTM E606 as shown in Fig. 2(a). Tests were performed at the room temperature with a 100 kN Instron servo-hydraulic test machine. Three specimens were tested; each subjected to a fully-reversed cyclic loading at a fixed constant strain amplitude of 1%, 1.5%, or 2%, at a frequency of 0.1 Hz. The stress and strain values were recorded at a frequency of 40 Hz until the cyclic hysteresis loops reached to a stabilised state.

2.3. Interrupted fatigue test with X-ray CT scanning

Load controlled fatigue test specimens were extracted from the porosity wall in vertical orientation with respect to the build direction and machined according to ASTM E466 standard as shown in Fig. 2(b). Three specimens were tested and referred to as Fatigue-Tomography (FT) specimens FT-1, FT-2 and FT-3. Specimen FT-1 was subjected to an interrupted fatigue test with six X-ray CT measurements. The first X-ray CT measurement was taken at the beginning of fatigue testing and the remaining five measurements were carried out at suitable intervals during the fatigue test. For specimens FT-2 and FT-3, X-ray CT scanning was performed at the start of the test, followed by fatigue test until failure.

The interrupted fatigue test set-up consisted of two units: a 50 kN load controlled fatigue test unit (Shimadzu) and an X-ray CT scanning unit (X TH 160 system, Nikon Metrology). The entire gauge section (5 mm diameter and 10 mm length) of the specimen was scanned by the X-ray CT to map the initial porosity distribution. Specimen FT-1 was then fatigue tested at an applied stress amplitude of 315 MPa, stress ratio of 0.1 and at a frequency of 20 Hz till 2×10^4 cycles which is approximately 65% of the expected fatigue life of the specimen based on the previous test results [33]. At this point, the fatigue test was interrupted to perform X-ray CT scanning, following which the fatigue test was resumed. Subsequent fatigue tests were interrupted at every few thousand cycles to perform X-ray CT scans. All the X-ray CT scans were conducted at an accelerating voltage of 120 kV, 58 μA current and voxel size of 20 μm (effective pixel size of 10 μm). Exposure time was set to 500 ms while capturing 1583 projections (rotation step size 0.22°), which resulted in each interrupted scan time of approximately 50 min. The scanned files were analysed using Volume graphics® software (VG Studio Max 2.2).

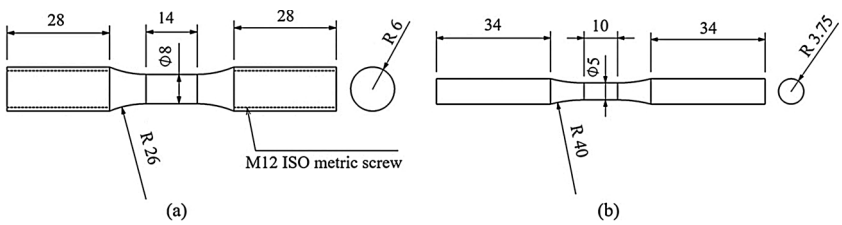

Fig. 2. Specimen geometry and dimensions for: (a) cyclic stress-strain test, (b) interrupted fatigue test with periodic X-ray computed tomography scanning.

3. Material properties and characteristics

3.1. Cyclic stress-strain curve

The cyclic stress-strain constitutive relationship of WAAM Ti-6Al-4 V was obtained from the displacement controlled cyclic load test described in Section 2.2. Changes in the cyclic deformation magnitude was more pronounced for the initial 20 cycles as shown in Fig. 3(a), owing to the rearrangement of the dislocation substructure [34]. Subsequently, the material stabilises and the stress vs. strain response at this stage can be used to represent the steady state cyclic deformation behaviour of the material or stabilised hysteresis loop at a given load. gives the cyclic strength coefficient and cyclic strain hardening exponent respectively. It should be mentioned that the engineering stress and strain values were used instead of the true stress and strain values because cyclic hysteresis loops were measured at low strain levels (up to 2%) where the difference between true and engineering stress and strain values are negligible [39].

$$\frac{\Delta\varepsilon}{2} = \frac{\Delta\sigma}{2E} + \left(\frac{\Delta\sigma}{2K'}\right)^{\frac{1}{n'}} \tag{1}$$

where $\Delta\varepsilon$ is the applied strain range, $\Delta\sigma$ the stress range, K' the cyclic strength coefficient and n' the cyclic strain hardening exponent. The values are provided in Table 2.

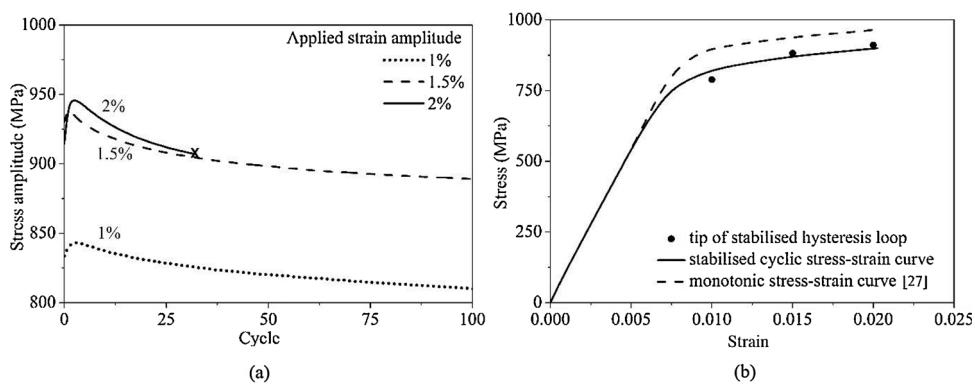

Fig. 3. (a) Cyclic softening behaviour, (b) stabilised cyclic stress-strain curve of WAAM Ti-6Al-4 V. Note: strain at failure for monotonic stress-strain curve is 0.12 ± 0.02, which is outside the scale of (b).

Table 2
Cyclic properties of WAAM Ti-6Al-4V.

Modulus of elasticity, E (GPa)	Cyclic strength coefficient K' (MPa)	Strain hardening exponent n'	Fatigue strength coefficient σ_f' (MPa)	Fatigue strength exponent b
116	1582	0.125	1470	−0.068

The material showed cyclic hardening behaviour for the first 3 to 4 cycles, followed by cyclic softening response for the remaining test cycles. This behaviour can be attributed to the lamellar morphology of the α grains present in the colony and Widmanstätten arrangement, which have been reported to cause initial hardening effect and followed by an overall cyclic softening effect [35]. It was also observed that the extent of softening in WAAM Ti-6Al-4V was less than the softening reported for the selective laser melted [36,37] and wrought Ti-6Al-4V [28,38]. The reason for this is that cyclic softening is primarily associated with the plastic deformation of the soft α phase. The lamellar morphology of α grains and the surrounding hard β matrix in WAAM Ti-6Al-4V assist in pinning down the movement of dislocations [35], thereby resulting in only 5 to 6% reduction in the peak stress (softening) with increase in number of cycles.

The stabilised cyclic stress-strain curve is shown in Fig. 3(b). The material showed cyclic softening in comparison to the monotonic stress-strain curve published in [33]. The cyclic stress vs. plastic strain plot was used to determine the material constants in the Ramberg–Osgood relationship in Eq. (1). The coefficient and slope of the best-fit curve

3.2. S–N curve

Intrinsic material property constants for the Basquin equation, Eq. (2), were estimated from the authors' previous result obtained by testing defect-free specimens [33], as shown in Fig. 4. S-N data (tested at stress ratio 0.1) was converted to another set of data corresponding to stress ratio of −1 using Walker's relation as shown in Eq. (3) [40], and then the applied stress amplitude vs. fatigue life was plotted in a logarithmic scale to determine the fatigue strength coefficient and fatigue strength exponent values, as shown in Table 2.

$$\sigma_a = \sigma'_f\,(N)^b \tag{2}$$

where σ_a is the applied stress amplitude, σ_f' the fatigue strength coefficient, N the cycles to failure, and b the fatigue strength exponent.

$$\sigma_e = \sigma_{max}\left(\frac{1-R}{2}\right)^{0.28} \tag{3}$$

where σ_e is the equivalent stress amplitude at a stress ratio of −1, under the applied maximum stress, σ_{max}, and applied stress ratio, R.

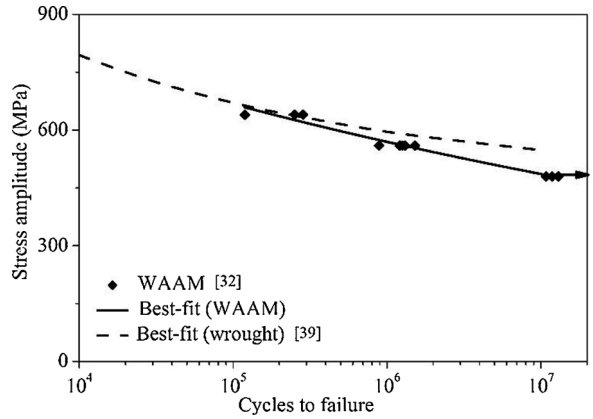

Fig. 4. S-N curve for WAAM Ti-6Al-4 V ($R = -1$) converted from test data at $R = 0.1$ by Eq. (3). Wrought Ti-6Al-4 V data at $R = -1$ from [41].

3.3. Porosity characterisation

Porosity size and distribution play an important role in fatigue life, particularly when pores are close to the surface and/or pore sizes are larger than the surrounding microstructural dimensions [42]. Therefore, the initial spatial distribution of the pores was obtained from X-ray CT scanning. The material density in all the specimens was 99.96 ± 0.005%. The pores observed in Fig. 5 had a spherical geometry and a pore size distribution of 206 ± 80 μm. In terms of location, pores were observed on surface, sub-surface and internal locations. Defect distribution in the porosity specimens did not show any noticeable change with respect to the distance from the substrate plate during WAAM material building (refer Fig. 1b), i.e. location did not seem to have affected the probability of porosity defect formation. However, this observation is not representative of the realistic (accidental) porosity distribution, as the porosity specimens used in this study were built on purpose using selective contamination at the specimen gauge section.

It is worth mentioning that in some cases X-ray CT scans included indistinct features of dimensions close to the resolution limit, which is manifested as scattered dots, visible in Fig. 5(c). Due to the uncertainty of such measurements, those data points were treated as artifacts in this study and therefore were excluded when performing porosity density calculations.

4. Life prediction method

4.1. Linear elastic stress analysis

Fig. 6(a) shows the X-ray CT image of the spatial distribution of pores in the gauge section of Specimen FT-1. X-ray CT scan is particularly useful for modelling the actual pore morphology and distribution of pores using image based FE analysis. However, due to computational limitations, instead of modelling the entire gauge length, only a selected volume of the gauge section was modelled, Fig. 6(a). The data was then processed (sectioned and meshed) using the Simpleware® software as shown in Fig. 6(b). Quadratic tetrahedron element of 10 nodes was selected, with typical number of elements being 20 around a pore and gradually reducing in number for sites away from the pore, thereby resulting in approximately 2×10^5 finite elements in the model.

Considering the computational cost involved with X-ray CT image based FEA, a comparative study was performed using an assumed isolated pore geometry as shown in Fig. 6(c), such that the location and size correspond a critical pore from the X-ray CT image. The stress concentration factor value obtained from the two models, i.e, (i) FE model with pore geometry from the X-ray CT image (Fig. 6b), and (ii) FE model with idealised pore geometry (Fig. 6d), were compared to determine the difference between the two models.

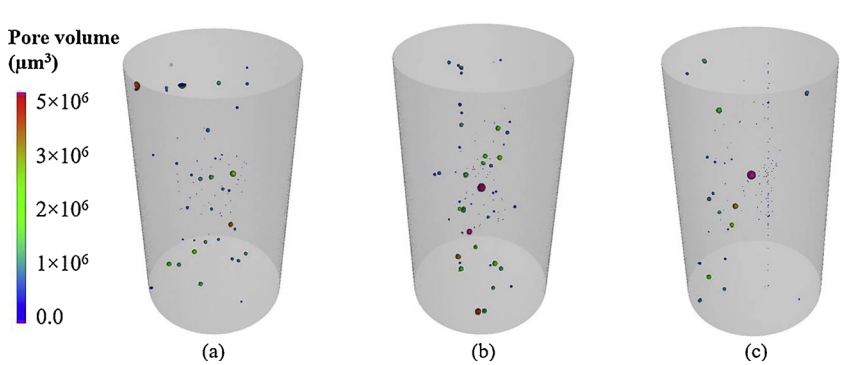

Fig. 5. X-ray computed tomography scans before fatigue testing: (a) Specimen FT-1 (used for interrupted fatigue-tomography test), (b–c) Specimens FT-2 and FT-3 (used for S-N test).

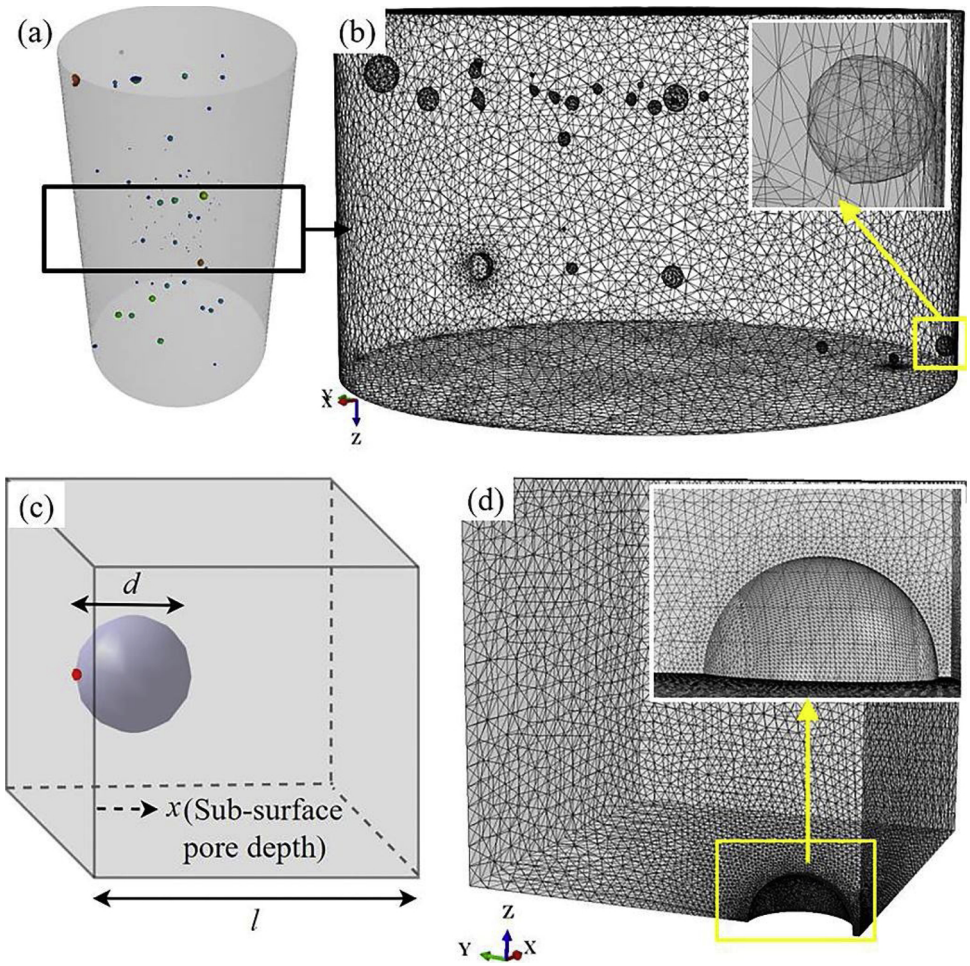

Fig. 6. (a) X-ray CT image of Specimen FT-1, (b) FE mesh of a reduced section of specimen gauge section taken from X-ray CT, (c) schematic of a sub-surface pore modelled with idealised geometries and symmetry boundary condition, (d) FE mesh of the idealised sub-surface pore.

4.2. Elastic-plastic cyclic load analysis

The stress-strain constitutive relation under cyclic load was modelled with a commercial software ABAQUS using a mixed isotropic-kinematic hardening model with the von Mises yield criterion as shown in Eq. (4). Details of the kinematic and isotropic hardening models are discussed in a previous study [32]. In general, under cyclic loading, the localised plastic zone at a pore root is subjected to displacement controlled loading condition owing to the constraint effect of the surrounding material which is subjected to elastic loading conditions. Therefore, the model was calibrated (Fig. 7) using the stabilised hysteresis loops for WAAM Ti-6Al-4V obtained from a fully reversed displacement controlled cyclic load test as described in Section 3.1.

$$F = f(\sigma - \alpha) - \sigma^0 \tag{4}$$

$$\alpha_k = \frac{C_k}{\gamma_k}(1 - e^{-\gamma_k \varepsilon^{pl}}) + \alpha_{k,1} e^{-\gamma_k \varepsilon^{pl}} \tag{5}$$

$$\sigma^0 = \sigma_0 + Q_\infty (1 - e^{-b\bar{\varepsilon}^{pl}}) \tag{6}$$

where f represents the von Mises stress function, α is the back-stress and σ° the yield stress. Five back-stresses were used in the kinematic model as shown in Eq. (5), which was expressed in terms of the modulus in the plastic region (C_k), and the rate of decrease (γ_k) in modulus with increased plastic strain (ε^{pl}). The reduction in the yield stress in the isotropic model (Eq. (6)), was expressed in terms of the maximum change in the value of yield stress (Q_∞) and the rate of decrease of yield stress (b) with an increase in equivalent plastic strain ($\bar{\varepsilon}^{pl}$). The calibrated model parameters are given in Table 3.

Elastic analysis showed that the FE model built from the X-ray CT scan input requires 2×10^5 elements for a converged mesh. Running such a model for cyclic analysis would require excessive memory allocation and would generate a very large output file (about 50GB) which would be difficult to analyse. Therefore, based on the stress concentration factor value obtained from elastic FE analysis under static load, the critical pore in the gauge section was identified and modelled using the nearest ideal pore geometry assumption such that the stress concentration factor value was within ± 1% of the value of stress concentration factor obtained from the X-ray CT scanned pore geometry model.

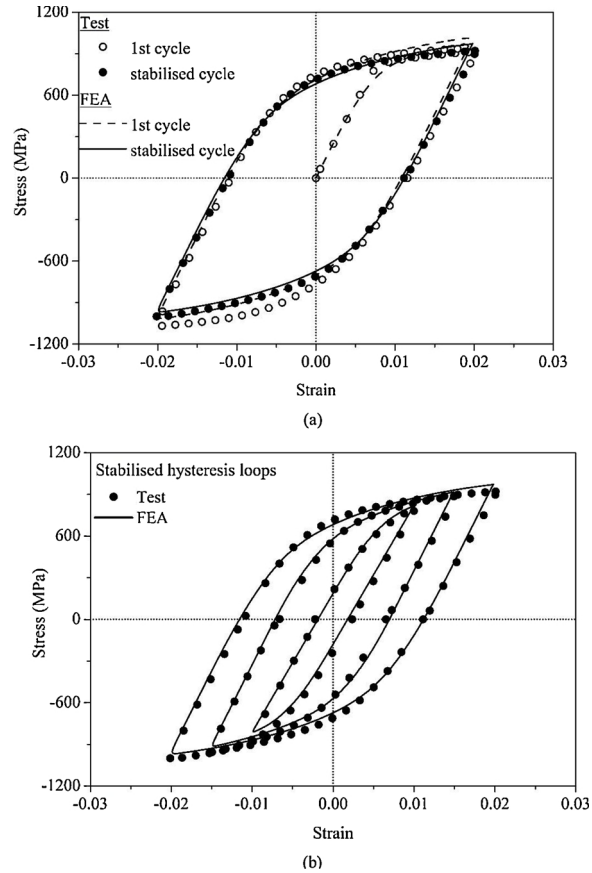

Fig. 7. Calibration of the mixed isotropic-kinematic hardening model with stabilised hysteresis loops from experimental test: (a) first cycle and stabilised cycle, (b) stabilised hysteresis loops at 1%, 1.5% and 2% fully reversed applied strain amplitudes for WAAM Ti-6Al-4V.

Table 3
Mixed kinematic (C_k, GPa; γ_k) and isotropic (Q, MPa; b) model parameters fitted to stabilised hysteresis loops for WAAM Ti-6Al-4 V obtained from cyclic load test.

C_1	γ_1	C_2	γ_2	C_3	γ_3	C_4	γ_4	C_5	γ_5	Q_∞	b
95	2000	52	1200	35	850	22	100	6.8	50	−100	0.5

4.3. Fatigue life prediction

Pores lead to a stress concentration effect at the in a way similar to notches. The pore root is therefore subjected to a higher stress amplitude such that the maximum stress can be above the yield stress of Ti-6Al-4V. Subsequently, local plastic deformation takes place and the cyclic softening effect leads to a reduction in local maximum stress at the pore root. Since the fatigue life is inversely proportional to the stress amplitude and mean stress, it can be inferred that considering the effect of stress concentration without the mean stress relaxation will lead to a highly conservative prediction. Therefore, mean stress relaxation was determined from FE analysis with the cyclic plasticity model. It was assumed that the fatigue life of the specimen is controlled by the local stress amplitude and local mean stress (in terms of the stress ratio) at the pore root, which was calculated from FE analysis. The local stress amplitude and stress ratio were then converted to equivalent stress amplitude at a stress ratio of −1 (mean stress is zero) using Eq. (3). The equivalent stress amplitude was used for fatigue life prediction using the Basquin equation (Eq. (2)).

5. Results and discussion

5.1. X-ray tomography measurements

Porosity growth under cyclic loads was confirmed from the interrupted fatigue-tomography test results as shown in Fig. 8(a). Porosity growth was observed at every scan interval, with the maximum growth seen between 2×10^4 cycles and 2.8×10^4 cycles which is 65–85% of the total fatigue life of the specimen. This can be due to the high stress concentration at the pore root ($K_t \geq 2$) which leads to a localised plastic deformation. Slip lines, which are a manifestation of cyclic plastic deformation, were observed in one of the specimens. The crack initiation site (Fig. 8b) showed persistent slip bands on the pore surface near the regions close to the highest stress concentration point as shown in Fig. 8(c). In addition to being a stress raiser, pores also provide a free surface for the dislocations to pile up [13], which causes the material to move away from the pore surface and therefore can lead to an increase in the pore diameter and morphology evolution. Fig. 9 shows the changes in the pore morphology with fatigue loading cycles.

Further, it was observed that fatigue crack was initiated from more than one pores at 70–80% of the fatigue life of the specimen. Since the tomography scans were taken at unloaded condition, it was difficult to image the entire crack. Fig. 10 shows that tortuous cracks originated preferentially at sub-surface pores in comparison to internal pores and grow towards the free surface of the specimen. The cracks originated at the mid-riff section of the pores. This can be explained by the higher value (about 25%) of stress concentration factor for sub-surface pores.

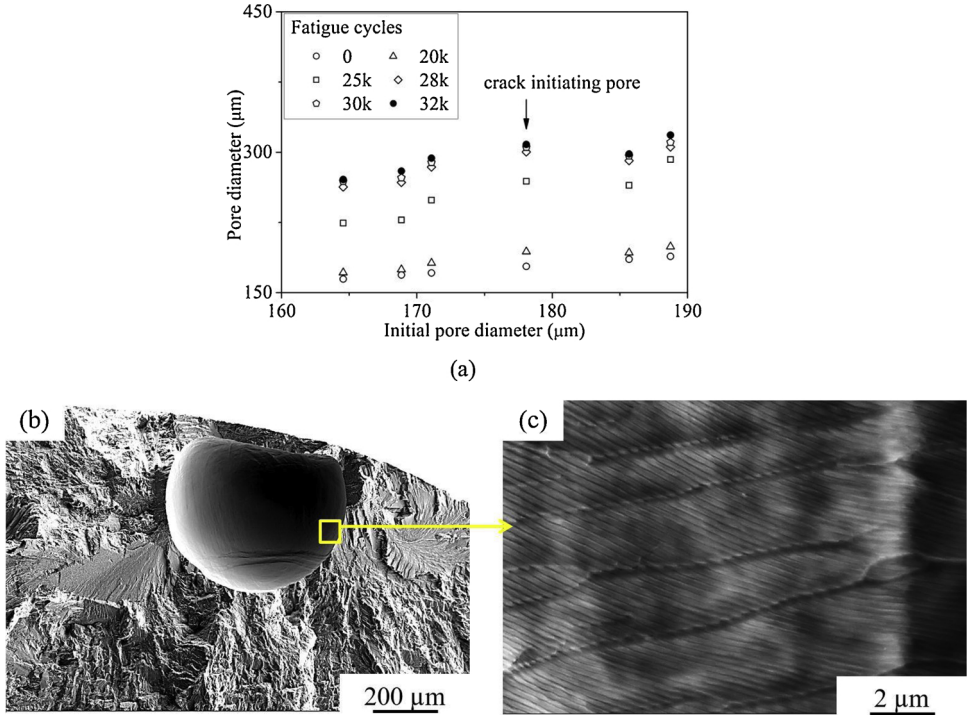

Fig. 8. (a) Increase in porosity diameter with fatigue cycles, (b) crack initiation at a pore (applied stress amplitude 315 MPa, stress ratio 0.1, fatigue life 2.46×10^4 cycles), (c) enlarged image of pore's internal surface showing slip lines indicating dislocation pile-up leading to fatigue damage initiation.

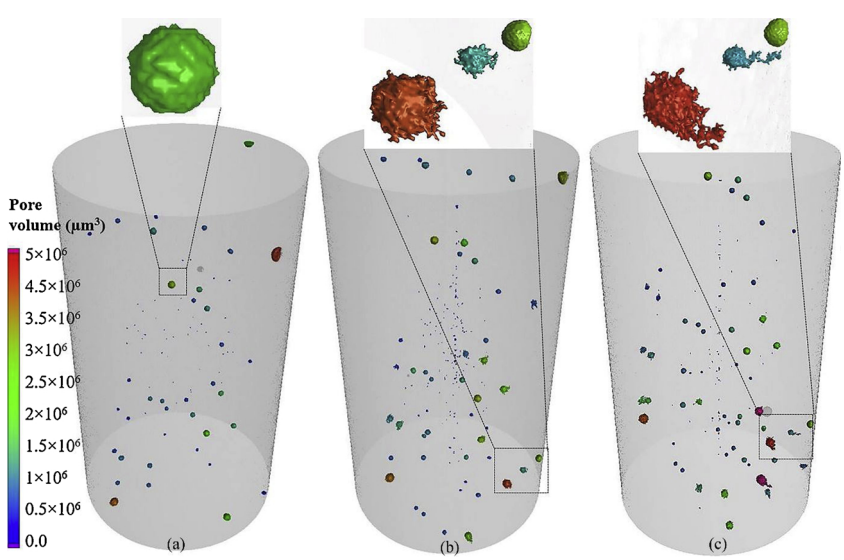

Fig. 9. Three dimensional view of X-ray CT scans of Specimen FT-1, showing the changes in pore morphology with accumulated fatigue cycles (N): (a) $N = 0$, (b) $N = 2.5 \times 10^4$, (c) $N = 3.2 \times 10^4$ (specimen failed at 32,380 cycles).

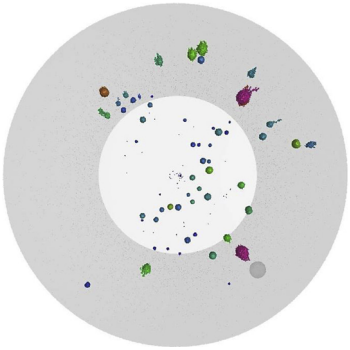

Fig. 10. X-ray CT image of the top view of Specimen FT-1 gauge section at 3.2×10^4 cycles, showing the tortuous cracks emerging from the near surface defects and growing towards the free surface.

5.2. Fatigue fracture surface

All the specimens showed crack initiation at isolated spherical pores located on the free surface of the specimen as shown in Fig. 11(a–c). It was found that the critical sub-surface pores identified in the initial X-ray CT scan had been transformed into surface pores. This is due to the collapse of the tiny ligament of material between the pore and the free surface [43].

The fatigue fracture surface was characterised by three distinct regions, (i) crack initiation and short crack growth region (within 0.5 mm to 1 mm radius around the gas pore) visualised as transgranular facets as shown in Fig. 11(d), (ii) rapid crack growth region manifested by ductile striations as shown in Fig. 11(e), and the final fracture region which was characterised by a dimple fracture behaviour as shown in Fig. 11(f). The crack initiating pore from the SEM image of the fracture surface was traced back to the initial X-ray tomography scan taken during the porosity characterisation studies presented in Fig. 5 (before application of fatigue loading). The crack initiating pore diameter measured from the fracture surface image was found to be approximately twice the pore diameter measured from the initial X-ray CT scan data.

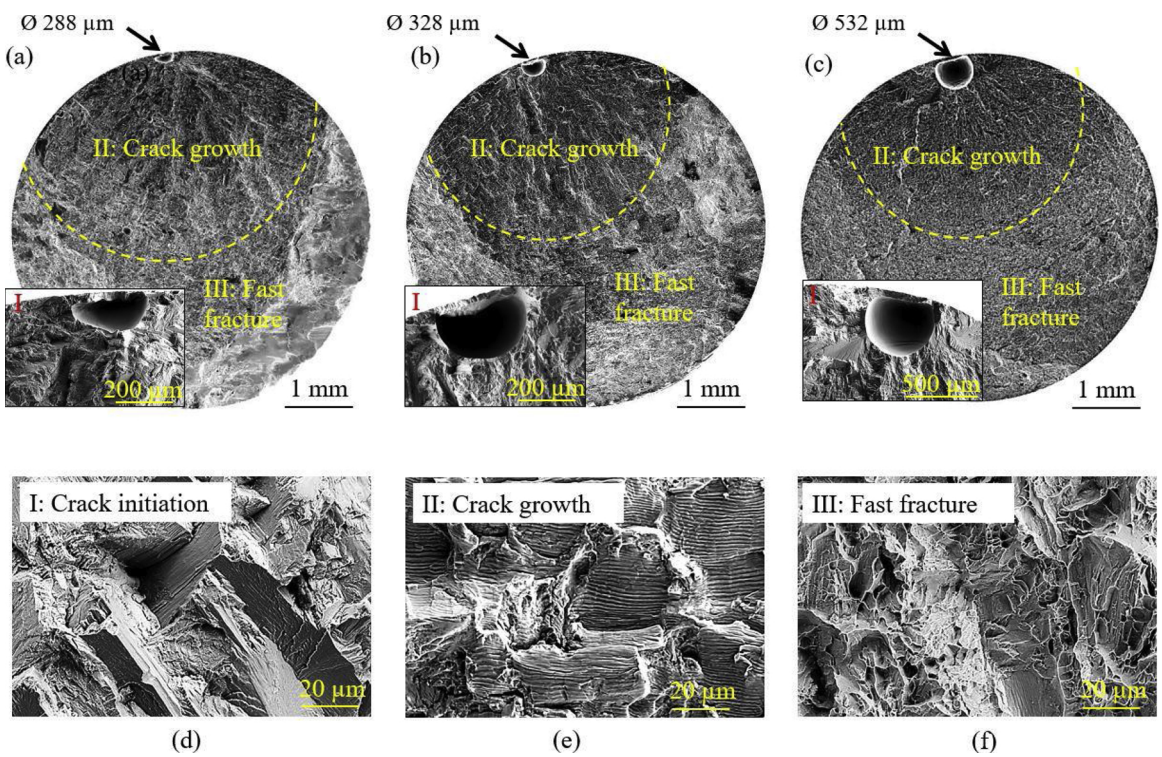

Fig. 11. SEM images of fatigue fracture surface of specimens: (a) FT-1, (b) FT-2, (c) FT-3, with enlarged view of the crack initiating pore at bottom left corner (note the different scale bars in the enlarged images); crack path morphology at: (d) crack initiation region (transgranular facets), (d) rapid crack growth region (striations), (e) fast or final fracture region (dimples).

5.3. Computational results

5.3.1. Stress concentration factor

Pore location refers to the distance of the pore from the free surface. Stress concentration factor (K_t) was calculated from the X-ray CT scanned pore geometry as shown in Fig. 12(a). For the various pores in the scanned volume, the variation in K_t with distance from the free surface is shown in Fig. 12(b). It can be seen that the results of the FE model built from the X-ray CT input conforms to the results of the FE model built from the ideal pore geometry assumptions. Location dominates the K_t for pores located within unit normalised distance (ratio of the distance of the pore from the free surface to the pore diameter). Fig. 12(a) also shows that for internal sites, the size and location of pores did not influence the value of K_t. This indicates that the load carrying cross-sectional area remains practically the same with a change in porosity size and location for internal pores.

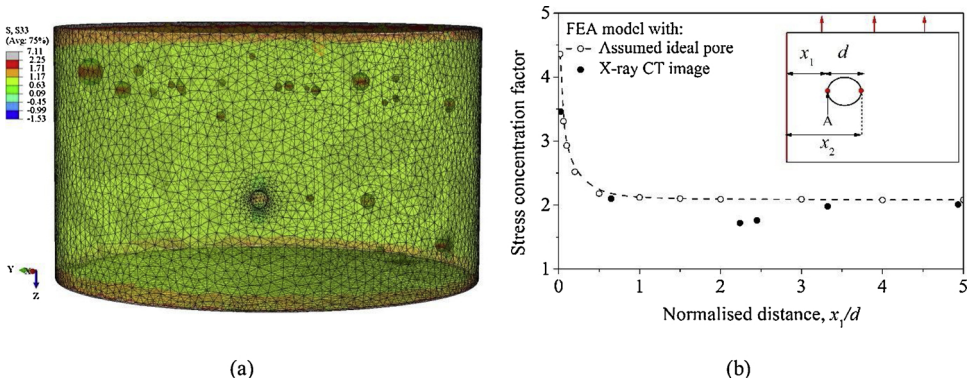

Fig. 12. (a) FE model using X-ray computed tomography (CT) scanned geometry, (b) variation in stress concentration factor (K_t) at pore root point 'A' with distance "x_1" from free surface, calculated using both idealised spherical pore geometry and X-ray CT scanned pore geometry.

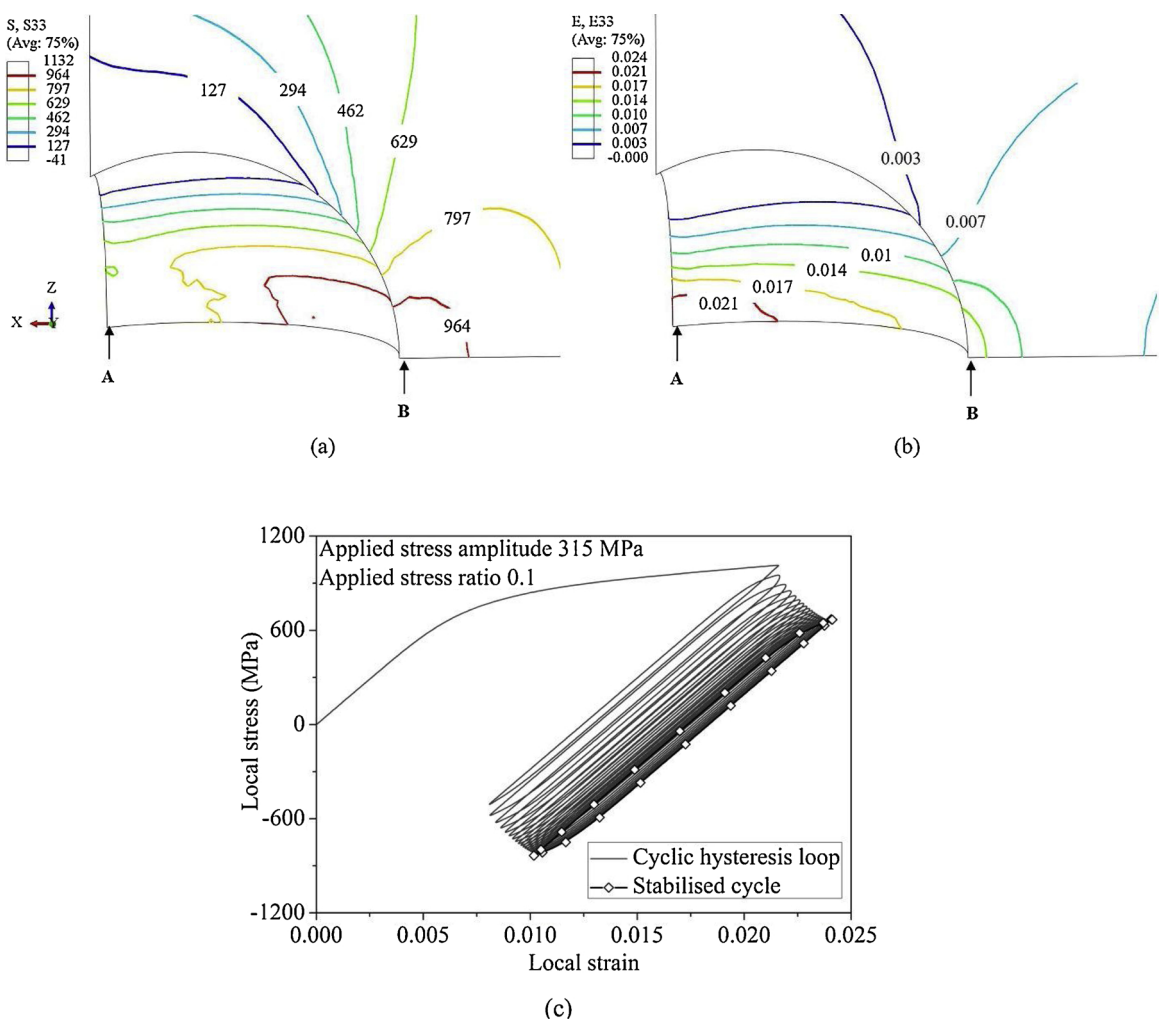

Fig. 13. Calculated stress and strain distributions at pore root by ¼ model (applied stress amplitude 315 MPa, stress ratio 0.1): (a) maximum stress at pore root, (b) maximum strain at pore mouth, (c) mean stress reduction at the pore mouth.

Table 4
Validation of FE model prediction with test data- X-ray CT and fracture surface analysis.

Pore diameter (μm) *pore dia. before test †pore dia. after test		Pore root depth, x_2, from surface (μm)	Normalised distance (x_2/d)	Fatigue life (test) (cycles)	Fatigue life (prediction) (cycles)	Error (%)
Tomography*	Fractography†					
162	288	144	0.5	3.23×10^4	2.9×10^4	10.2
229	328	240	0.7	2.37×10^4	2.2×10^4	7.17
241	534	430	0.8	2.46×10^4	2.2×10^4	10.5

Note: Pore diameter measured on the fracture surface was used in the cyclic plastic FE model.

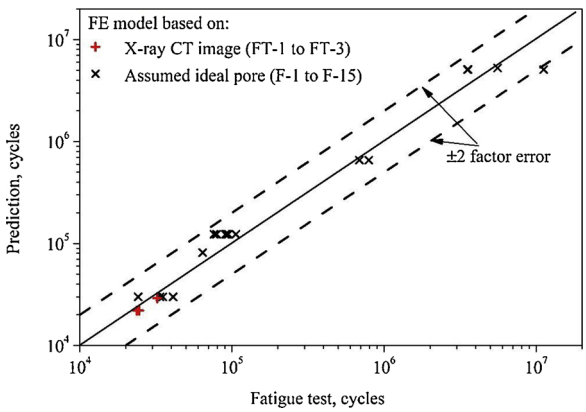

Fig. 14. Validation of fatigue life prediction method with tests conducted in this study, i.e. fatigue-tomography (FT) specimens FT-1 to FT-3, and a previous study using fatigue (F) test specimens F-1 to F-15 [33].

5.3.2. Cyclic strain accumulation at pore

The local stress and strain amplitude at the pore root was calculated from the cyclic plasticity model. Fig. 13(a) and (b) shows the local stress and strain distributions in the loading direction respectively. It can be seen that the maximum stress is at the root of the pore, while the maximum strain is at the free surface or the mouth of the pore. Fig. 13(c) shows the stress vs. strain calculated at the pore root. It can be seen that after a few initial ratcheting cycles, the stress vs. strain response stabilises.

5.3.3. Life prediction and validation

Local stress amplitude was calculated from the cyclic plasticity model and used in the Basquin equation (Eq. (2)) for fatigue life prediction using the procedures described in 4.3. Fatigue life predicted by the model corresponded with the test fatigue life as shown in Table 4.

For further validation, the assumed pore geometry was used for fatigue life prediction of specimens with crack initiating pores reported in a previous study [33] as shown in Fig. 14. These models were built from the SEM images of fatigue specimen's fracture surface. It can be seen that the error in the fatigue life prediction was higher when the prediction is based solely on information from fracture surface as opposed to when X-ray CT information is used in addition to fracture surface analysis (results in Table 4).

6. Conclusions

This study was aimed at investigating the change in the porosity morphology in wire + arc additive manufactured titanium alloy (WAAM Ti-6Al-4V) under fatigue loading. X-ray computed tomography (X-ray CT) measurements were taken at intervals during the fatigue testing. An image-based finite element (FE) model was established based on the X-ray CT information and compared to the modelling results based on idealised pore geometries. Cyclic plasticity model parameters were determined for WAAM Ti-6Al-4V and used to calculate the mean stress reduction at the pore root. The stress amplitude at the pore vicinity was used in the Basquin equation for fatigue life prediction. Key findings are summarised as the following:

(1) Finite element calculated stress concentration factor using idealised pore geometry is in good agreement with that obtained from image-based FE model using the X-ray CT input. This verifies using idealised pore geometries for FE modelling applications.
(2) Ten largest pores were monitored that approximately doubled their original size with increasing load cycles. Rapid increase in pore size was observed at about 65–85% of the total life of the specimen. Presence of fine slip lines on the pore internal surface indicates that the pores acted as free surfaces for accumulation of dislocations, hence grew during fatigue loading.
(3) Predicted fatigue life was within a factor of ± 2 when the model was based on inputs from the fracture surface analysis alone. Prediction accuracy was improved significantly (error about 10%) when FE model was informed by X-ray CT and fracture surface analysis.

Conflict of interest

We can confirm that this paper has not been published before and that all authors have approved the submission to this journal. We can confirm that there is no conflict of interest regarding the work that is presented in this paper.

Acknowledgement

We acknowledge UK Engineering and Physical Science Research Council (EPSRC) for financial support through the NEWAM Programme Grant EP/R027218/1. Romali Biswal thanks Coventry University for the PhD studentship.

References

[1] M. Seifi, A. Salem, D. Satko, J. Shaffer, J.J. Lewandowski, Defect distribution and microstructure heterogeneity effects on fracture resistance and fatigue behavior of EBM Ti-6Al-4V, Int. J. Fatigue 94 (2017) 263–287, https://doi.org/10.1016/j.ijfatigue.2016.06.001.
[2] S. Bagehorn, J. Wehr, H.J. Maier, Application of mechanical surface finishing processes for roughness reduction and fatigue improvement of additively manufactured Ti-6Al-4V parts, Int. J. Fatigue 102 (2017) 135–142, https://doi.org/10.1016/j.ijfatigue.2017.05.008.
[3] J. Günther, D. Krewerth, T. Lippmann, S. Leuders, T. Tröster, A. Weidner, H. Biermann, T. Niendorf, Fatigue life of additively manufactured Ti-6Al-4V in the very high cycle fatigue regime, Int. J. Fatigue 94 (2016) 236–245, https://doi.org/10.1016/j.ijfatigue.2016.05.018.
[4] M. Kahlin, H. Ansell, J.J. Moverare, Fatigue behaviour of notched additive manufactured Ti6Al4V with as-built surfaces, Int. J. Fatigue 101 (2017) 51–60, https://doi.org/10.1016/j.ijfatigue.2017.04.009.
[5] N. Hrabe, T. Gnaupel-Herold, T. Quinn, Fatigue properties of a titanium alloy (Ti-6Al-4V) fabricated via electron beam melting (EBM): effects of internal defects and residual stress, Int. J. Fatigue 94 (2015) 202–210, https://doi.org/10.1016/j.ijfatigue.2016.04.022.
[6] A.J. Sterling, B. Torries, N. Shamsaei, S.M. Thompson, D.W. Seely, Fatigue behavior and failure mechanisms of direct laser deposited Ti-6Al-4V, Mater. Sci. Eng. A 655 (2016) 100–112, https://doi.org/10.1016/j.msea.2015.12.026.
[7] F. Wang, S. Williams, P.A. Colegrove, A.A. Antonysamy, Microstructure and mechanical properties of wire and arc additive manufactured Ti-6Al-4V, Metall. Mater. Trans. A Phys. Metall. Mater. Sci. 44 (2013) 968–977, https://doi.org/10.1007/

s11661-012-1444-6.
[8] P.A. Colegrove, J. Donoghue, F. Martina, J. Gu, P. Prangnell, J. Hönnige, Application of bulk deformation methods for microstructural and material property improvement and residual stress and distortion control in additively manufactured components, Scr. Mater. 135 (2017) 111–118, https://doi.org/10.1016/j.scriptamat.2016.10.031.
[9] E. Brandl, F. Palm, V. Michailov, B. Viehweger, C. Leyens, Mechanical properties of additive manufactured titanium (Ti-6Al-4V) blocks deposited by a solid-state laser and wire, Mater. Des. 32 (2011) 4665–4675, https://doi.org/10.1016/j.matdes.2011.06.062.
[10] P. Åkerfeldt, M.L. Antti, R. Pederson, Influence of microstructure on mechanical properties of laser metal wire-deposited Ti-6Al-4V, Mater. Sci. Eng. A 674 (2016) 428–437, https://doi.org/10.1016/j.msea.2016.07.038.
[11] C.L.A. Leung, S. Marussi, R.C. Atwood, M. Towrie, P.J. Withers, P.D. Lee, In situ X-ray imaging of defect and molten pool dynamics in laser additive manufacturing, Nat. Commun. 9 (2018) 1–9, https://doi.org/10.1038/s41467-018-03734-7.
[12] B.E. Carroll, T.A. Palmer, A.M. Beese, Anisotropic tensile behavior of Ti-6Al-4V components fabricated with directed energy deposition additive manufacturing, Acta Mater. 87 (2015) 309–320, https://doi.org/10.1016/j.actamat.2014.12.054.
[13] S. Suresh, Fatigue of Materials, Chapter 3 and 7 (1998), https://doi.org/10.1017/CBO9780511806575.
[14] M. Benedetti, V. Fontanari, The effect of bi-modal and lamellar microstructures of Ti-6Al-4V on the behaviour of fatigue cracks emanating from edge-notches, Fatigue Fract. Eng. Mater. Struct. 27 (2004) 1073–1089, https://doi.org/10.1111/j.1460-2695.2004.00825.x.
[15] G. Lutjering, J. Williams, Engineering Materials and Processes – Titanium, 2nd ed., (2007) Chapter 5.
[16] P. Li, P.D. Lee, D.M. Maijer, T.C. Lindley, Quantification of the interaction within defect populations on fatigue behavior in an aluminum alloy, Acta Mater. 57 (2009) 3539–3548, https://doi.org/10.1016/j.actamat.2009.04.008.
[17] S. Tammas-Williams, P.J. Withers, I. Todd, P.B. Prangnell, The influence of porosity on fatigue crack initiation in additively manufactured titanium components, Sci. Rep. (2017) 1–13, https://doi.org/10.1038/s41598-017-06504-5.
[18] Y. Murakami, Metal fatigue: Effects of Small Defects and Nonmetallic Inclusions, 1st ed., Elsevier, 2002.
[19] I. Bantounas, D. Dye, T.C. Lindley, The effect of grain orientation on fracture morphology during high-cycle fatigue of Ti-6Al-4V, Acta Mater. 57 (2009) 3584–3595, https://doi.org/10.1016/j.actamat.2009.04.018.
[20] M.H. El Haddad, T.H. Topper, K.N. Smith, Prediction of non propagating cracks, Eng. Fract. Mech. 11 (1979) 573–584.
[21] L. Sheridan, O.E. Scott-Emuakpor, T. George, J.E. Gockel, Relating porosity to fatigue failure in additively manufactured alloy 718, Mater. Sci. Eng. A 727 (2018) 170–176, https://doi.org/10.1016/j.msea.2018.04.075.
[22] S. Leuders, M. Vollmer, F. Brenne, T. Tröster, T. Niendorf, Fatigue strength prediction for titanium alloy TiAl6V4 manufactured by selective laser melting, Metall. Mater. Trans. A 46 (2015) 3816–3823, https://doi.org/10.1007/s11661-015-2864-x.
[23] S. Beretta, S. Romano, A comparison of fatigue strength sensitivity to defects for materials manufactured by AM or traditional processes, Int. J. Fatigue 94 (2017) 178–191, https://doi.org/10.1016/j.ijfatigue.2016.06.020.
[24] S. Beretta, G. Chai, E. Soffiati, A weakest–link analysis for fatigue strength of components containing defects, Convegno IGF XVII Bol. 2004, (2008) http://www.gruppofrattura.it/ocs/index.php/cigf/igf17/paper/view/272/0.
[25] S. Siddique, M. Awd, J. Tenkamp, F. Walther, Development of a stochastic approach for fatigue life prediction of AlSi12 alloy processed by selective laser melting, Eng. Fail. Anal. 79 (2017) 34–50, https://doi.org/10.1016/j.engfailanal.2017.03.015.
[26] S. Romano, A. Brückner-Foit, A. Brandão, J. Gumpinger, T. Ghidini, S. Beretta, Fatigue properties of AlSi10Mg obtained by additive manufacturing: defect-based modelling and prediction of fatigue strength, Eng. Fract. Mech. 187 (2018) 165–189, https://doi.org/10.1016/j.engfracmech.2017.11.002.
[27] S. Romano, A. Brandão, J. Gumpinger, M. Gschweitl, S. Beretta, Qualification of AM parts: extreme value statistics applied to tomographic measurements, Mater. Des. 131 (2017) 32–48, https://doi.org/10.1016/j.matdes.2017.05.091.
[28] A. Thant, Y. Miyashita, Y. Otsuka, Y. Mutoh, S. Sakurai, Notch fatigue behavior of Ti-6Al-4V alloy in transition region between low and high cycle fatigue, Int. J. Fatigue 95 (2017) 194–203, https://doi.org/10.1016/j.ijfatigue.2016.10.024.
[29] G. Härkegård, Short-crack modelling of the effect of corrosion pits on the fatigue limit of 12% Cr steel, Fatigue Fract. Eng. Mater. Struct. 38 (2015) 1009–1016, https://doi.org/10.1111/ffe.12305.
[30] D.F. Socie, J. Morrow, W.C. Chen, A procedure for estimating the total fatigue life of notched and cracked members, Eng. Fract. Mech. 11 (1979) 851–859, https://doi.org/10.1016/0013-7944(79)90142-5.
[31] M. Benedetti, C. Santus, Notch Fatigue and Crack Growth Resistance of Ti-6Al-4V ELI Additively Manufactured via Selective Laser Melting: A Critical Distance Approach to Defect Sensitivity, Elsevier Ltd., 2018, https://doi.org/10.1016/J.IJFATIGUE.2018.12.020.
[32] R. Biswal, A.K. Syed, X. Zhang, Assessment of the effect of isolated porosity defects on the fatigue performance of additive manufactured titanium alloy, Addit. Manuf. 23 (2018) 433–442, https://doi.org/10.1016/j.addma.2018.08.024.
[33] R. Biswal, X. Zhang, A.K. Syed, M. Awd, J. Ding, F. Walther, S. Williams, Criticality of porosity defects on the fatigue performance of wire + arc additive manufactured titanium alloy, Int. J. Fatigue 122 (2019) 208–217, https://doi.org/10.1016/j.ijfatigue.2019.01.017.
[34] R.W. Hertzberg, Deformation and Fracture Mechanics of Engineering Materials, 5th ed., Wiley, 2012 Chapter 9.
[35] F. Han, B. Tang, H. Kou, J. Li, Y. Deng, Y. Feng, Cyclic softening behavior of Ti–6Al–4V alloy at macro and micro-scale, Mater. Lett. 185 (2016) 115–118, https://doi.org/10.1016/j.matlet.2016.08.119.
[36] A. Phaiboonworachat, K.I. Kourousis, Cyclic elastoplastic behaviour, hardness and microstructural properties of Ti-6Al-4V manufactured through selective laser melting, Int. J. Mater. Eng. Innov. 7 (2016) 80–87, https://doi.org/10.1504/IJMATEI.2016.077324.
[37] D. Agius, K.I. Kourousis, C. Wallbrink, T. Song, Cyclic plasticity and microstructure of as-built SLM Ti-6Al-4V: the effect of build orientation, Mater. Sci. Eng. A 701 (2017) 85–100, https://doi.org/10.1016/j.msea.2017.06.069.
[38] P.E. Carrion, N. Shamsaei, S.R. Daniewicz, R.D. Moser, Fatigue behavior of Ti-6Al-4V ELI including mean stress effects, Int. J. Fatigue 99 (2017) 87–100, https://doi.org/10.1016/j.ijfatigue.2017.02.013.
[39] R.I. Stephens, A. Fatemi, R.R. Stephens, H.O. Fuchs, Metal Fatigue in Engineering, 2nd ed., (2000) Chapter 5-6.
[40] P. Li, D.H. Warner, A. Fatemi, N. Phan, Critical assessment of the fatigue performance of additively manufactured Ti-6Al-4V and perspective for future research, Int. J. Fatigue 85 (2016) 130–143, https://doi.org/10.1016/j.ijfatigue.2015.12.003.
[41] Metallic Materials Properties Development and Standardization, (2008) Chapter 5.
[42] R.K. Nalla, B.L. Boyce, J.P. Campbell, J.O. Peters, R.O. Ritchie, Influence of microstructure on high-cycle fatigue of Ti-6Al-4V: bimodal vs. Lamellar structures, Metall. Mater. Trans. A 33 (2002) 899–918, https://doi.org/10.1007/s11661-002-1023-3.
[43] S. Beretta, S. Romano, A comparison of fatigue strength sensitivity to defects for materials manufactured by AM or traditional processes, Int. J. Fatigue 94 (2017) 178–191, https://doi.org/10.1016/j.ijfatigue.2016.06.020.